2024-01-2078 Published 09 Apr 2024

Formula 1 Race Car Aerodynamics: Understanding Floor Flow Structures and Why It Is a Key Component in Modern Racing

Amr Shaalan and Dimitris Assanis Stony Brook University

Aditya Raman, Sameera Wijeyakulasuriya, and Kelly Senecal Convergent Science Inc.

Citation: Shaalan, A., Assanis, D., Raman, A., Wijeyakulasuriya, S. et al., "Formula 1 Race Car Aerodynamics: Understanding Floor Flow Structures and Why It Is a Key Component in Modern Racing," SAE Technical Paper 2024-01-2078, 2024, doi:10.4271/2024-01-2078.

Received: 10 Nov 2023 Revised: 26 Jan 2024 Accepted: 26 Jan 2024

Abstract

This paper delves into the intricate realm of Formula 1 race car aerodynamics, focusing on the pivotal role played by floor flow structures in contemporary racing. The aerodynamic design of the floor of a Formula 1 car is a fundamental component that connects the flow structures from the front wing to the rear end of the car through the diffuser, thus significantly influencing the generation of lift and drag. In this work, CFD was used to predict the structure of the vortices and flow pattern underneath a Formula 1 car using a CAD model that mimicked the modern Red Bull Racing Team's car in recent years. Through comprehensive analysis and simulation, a detailed understanding of the complex flow patterns and aerodynamic phenomena occurring beneath the floor of the car and its vicinity is presented. This entails a close examination of how air interacts with the floor of the car and how the flow around the car can be manipulated to alter the flow rate and the quality of air going into the diffuser, generating crucial insights into the underlying principles at play. Finally, special attention was focused on the tire squish area and the resulting structures affecting the diffuser. Vortex structures were illustrated utilizing volume renders of vorticity and velocity in the domain, alongside Velocity-based Line Integral Convolution (LIC) total pressure contours at the diffuser. The assessment was carried out for three different speeds of 30 *m/s*, 50 *m/s*, and 90 *m/s* with two different ride heights for each speed. This research aims to shed light and understand the critical factors that engineers and designers consider when optimizing Formula 1 race car aerodynamics, how different geometric elements interact, and why it is considered a difference maker in modern racing.

Introduction

The world of motorsport racing aerodynamics is a mesmerizing area where engineering excellence and innovation meet the relentless pursuit of speed. Modern racing has become intrinsically linked to the ever-evolving field of aerodynamic design. As Formula 1 cars slice through the air at astonishing speeds and incredible precision, one truth becomes abundantly clear: aerodynamics is the critical differentiator on race day. Formula 1 teams go to great lengths to hide the aerodynamics recipe incorporated in the designs from competitors, leaving almost nothing for the public to explore.

In 2013, a rare publication by a Formula 1 team, Sauber [1], illustrated the huge role that aerodynamics plays in Formula 1. Table 1 shows the identified contribution of each major component to downforce and drag from the study, where 53% of the total downforce generated was attributed to the floor and the diffuser. This highlights the crucial role that the floor plays in generating downforce and why Formula 1 teams allocate significant resources to its development. This task, however, is far from straightforward. For instance, if the floor geometry is kept unchanged and a modification is made on the front wing

TABLE 1 Downforce and drag forces breakdown in a 2009 Formula 1 car, adapted from W. Toet [1]

Component	Downforce (%)	Drag (%)
Front Wing	28.5	20
Front Wheel, Suspension, Brake Duct	-1	10
Chassis & Body Work	-8	10
Floor & Diffuser 53	13.5	
Rear Wheel, Suspension, Brake Duct	2	17.5
Front Wing	25	29

then the contribution of the floor could change in either direction. This is not only limited to upstream components, but a change in downstream components, like the rear wing assembly, can also have a marked effect. This is because the floor covers a significant area and connects the front and rear ends of the car; which in turn adds a significant complexity to its development process [3].

The goal to reduce drag on a race car is straightforward and intuitive. But a fair question would be why is downforce important? Downforce, or negative lift, generates a form of drag known as induced drag. The total drag is expected to follow Equation 1. For an airfoil, C_{D0} is defined as the parasite drag which is any drag that is not associated with lift generation. Note that the induced drag can be seen to correlate with the square of the coefficient of lift. In motorsport racing, such clear definitions are hard to pinpoint and as a result C_{D_0} and C_{L_0} would refer to the lift without some major components like the rear and front wing [3].

$$C_D = C_{D_0} + k\left(C_L + C_{L_0}\right)^2 \tag{1}$$

$$C_D = \frac{Drag\ Force}{\frac{1}{2}\rho_{ref} V_{ref}^2 A_{ref}} \tag{2}$$

Where C_D is the Total Drag Coefficient, C_{D_0} is the Parasite Drag Coefficient, C_L is the Lift Coefficient, C_{L_0} is the Lift Coefficient at 0 angle of attack, k is an experimentally-determined coefficient that correlates lift and drag generation, ρ_{ref} is the Reference Density, V_{ref} is the reference velocity, A_{ref} is the Reference Area

Downforce will also increase the friction produced from the free wheels on the car, which are the front wheels in the case of a rear wheels-driven Formula 1 car, and a reduction in the friction coefficient that is going to affect the driving wheel, which collectively will impede the speed of the car [1, 3]. It is then clear that lift generation is always coupled with drag generation. This would be a significant penalty that has to be endured during straight sectors of the race track; however, corners are where downforce is most useful.

The benefits gained from the downforce can be summarized by Figure 1 where an increase in the vertical load F_z directly translates into an increase in the lateral force F_y at a given slip angle β resulting in more turning force pushing the car faster into the corner. This is represented by moving from point A to C in the figure. Similarly, less slip angle is required to achieve the same lateral force when the vertical load is increased, represented by points A and B in the figure. This vertical load increase can be achieved by increasing the weight of the car. However, with that added inertia more power is going to be needed to propel the car. Providing this load aerodynamically, in the form of downforce, gives the car the advantage of adding vertical load without paying the penalty of the added inertia. This of course is only true if the drag force generated is not equivalent to the weight that needs to be added to achieve the same vertical load.

FIGURE 1 Effect of downforce on slip angle and turning of the car during cornering from Katz [2]

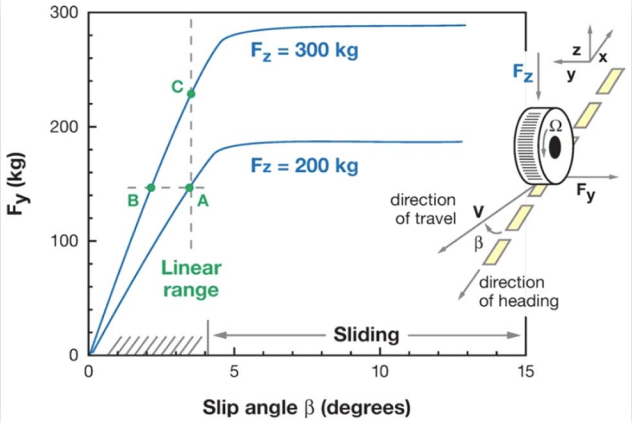

To illustrate the role of downforce in a race, Figure 2 shows a typical racing line of a Formula 1 car on a track during cornering. Achieving this racing line would require significant lateral force to be able to turn the car to follow the desired racing line and hit the apex of the corner, achieving faster speeds at the end of the corner, hence reducing total lap time. It is important to appreciate that while the car can be designed to generate the downforce required for cornering at a given track, this can change from one track to another. Therefore, the aerodynamic configuration of the car is expected to vary from one race track to another.

As mentioned earlier, the floor of the car is the biggest downforce-generating device on the car. Therefore, carefully designing this component is essential. One of the main tools that help refine the design to be in aerodynamic harmony with the other aerodynamic components is computational fluid dynamics (CFD) simulations that can replicate the complicated floor structure occurring on track. The concept of operation of the floor

FIGURE 2 Illustration of a racing line during cornering

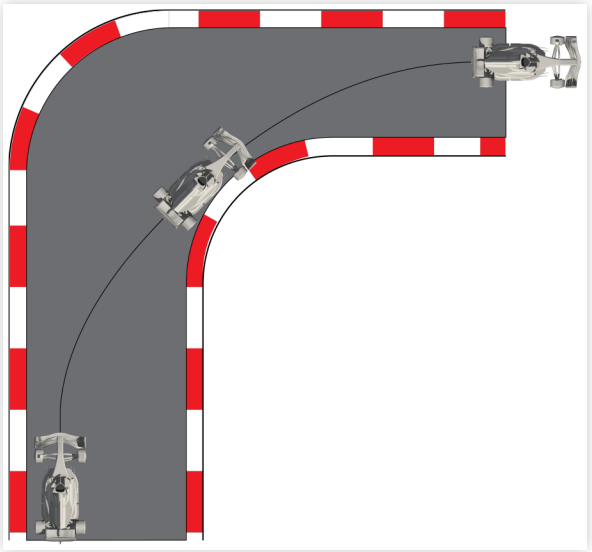

and the reason it generates significant downforce is its ability to rapidly increase the speed of the flow underneath the car. The floor creates a venturi flow that creates a low-pressure-high-speed zone that eventually expands in the diffuser at the end of the floor [3]. The diffuser expands the flow underneath the car to the pressure of the ambient flow. This pumping effect contributes further to the acceleration of the flow underneath the car. In fact, simulating these events in CFD has been shown to require accounting for compressibility effect to avoid significant errors that reached 18.69% in C_L and 11.24% in C_D estimations when using a scaled model to correlate with the wind tunnel model; this is caused by a Mach number mismatch as a result of matching the Reynolds Number where the speed would have to be increased to nullify the decrease in the model size [4].

One of the most important concepts that modern race cars rely on is controlling the flow using vortices that have been designed to shed at a specific location that adds significant benefits to the overall performance of the car. A vortex consists of a central region of reduced pressure surrounded by an outer region of increased pressure. Understanding the mechanics of vortices becomes clearer upon examining the concept of a vortex ring. In a vortex ring, the rotating air exerts an outward force driven by centrifugal effects, causing a drop in pressure at its core. Simultaneously, the stationary high-pressure air attempts to counteract this centrifugal force by moving toward the low-pressure area. Since angular momentum is conserved, the air follows a spiral path as it moves toward the center of the vortex [5, 6, 7].

$$\vec{\omega} = \vec{\nabla} \times \vec{V} \tag{3}$$

Where $\vec{\omega}$ is the Vorticity Vector, $\vec{V}$ is the Velocity Vector

Vorticity, defined as the curl of the velocity as shown in Equation 3, is an important indicator of the location of vortices and how they behave. Controlling vortices at various locations around the car is pivotal to the performance of the car. Generally, vortices are lossy and can cause an increase in drag. Nonetheless, vortices make up for this loss by entraining the flow and guiding it through more favorable routes that would have alternatively caused even more drag and less downforce, thus cumulatively resulting in a higher downforce-to-drag ratio. One example where this is most apparent is the use of vortices to seal the floor. Generally, the floor of the car is desired to maintain a low pressure (suction) to generate downforce. This low pressure would be hindered if highly turbulent flow went underneath the car from the sides. Therefore, vortices aim to guide the outer flow from infiltrating underneath the car at undesirable locations. Another example is the use of vortices generated from the front wing to control the deflected flow from the tires laterally underneath the car, or into the rear diffuser in the case of rear tires, known as tire squirt. One of the most commonly referred to vortices that played a significant role in that regard is known as the "Y-250" vortex, named after the inboard edge of the front wing elements from where the vortex is shed, which certain front-wing geometries allowed in previous regulations [8].

This work is dedicated to explaining the nature of the flows that arise from the floor and the challenges that come with it. In a field where publications are scarce due to the secretive nature of the competition, a computational effort is sought to thoroughly discuss important aerodynamics phenomena leveraged for performance by Formula 1 racing teams. The geometry used, albeit approximate, enhances this understanding by offering visual aids using advanced postprocessing techniques like Volume Rendering and Line Integral Convolution (LIC) that represent the typical flow patterns and structures seen on an actual Formula 1 racing car.

Computational Model Setup

CAD Model

The Computer-Aided Design (CAD) model built for this analysis was based on a model published online [9] that aimed to copy a variant of the Oracle Red Bull Racing car in the 2022 season, *RB18*. The original CAD model, shown in Figure [3], was extremely detailed with the internal components included. It is also unknown whether the purpose of the published CAD model was aerodynamic efficiency, but there were some indications that it was an attempt to replicate the overall looks of the geometry. For instance, the front and rear wings alongside the rest of the aerodynamic surfaces did not always have an airfoil shape but were instead sometimes simplified to rounded-edge curved plates. It is also worth mentioning that the design of the surfaces and aerodynamic components on the car requires a very complicated approach to ensure optimal performance, like aligning the bargeboards and strakes with the incident flow. Such attempts are practically impossible to replicate just by looking at published

FIGURE 3 Original unmodified CAD model as found in [9]

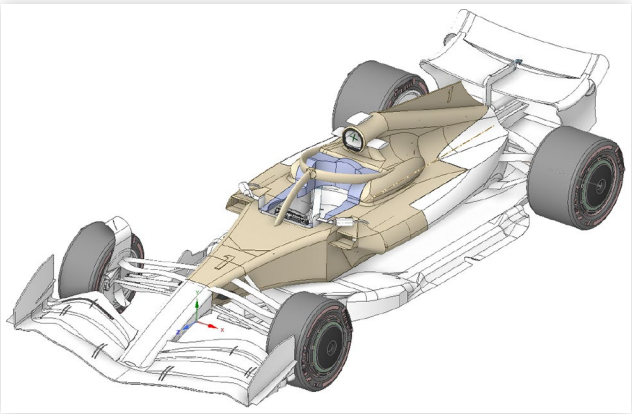

FIGURE 4 Cleaned model of the car compared with a variation of the floor of the RB18

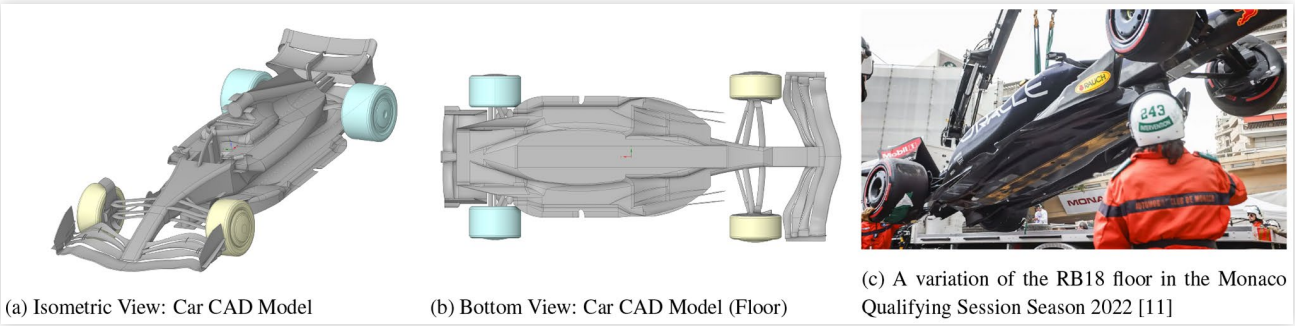

(a) Isometric View: Car CAD Model (b) Bottom View: Car CAD Model (Floor) (c) A variation of the RB18 floor in the Monaco Qualifying Session Season 2022 [11]

images from events and would require extensive CFD analysis and wind tunnel testing. Therefore, it is not expected of this CAD model to produce aerodynamic efficiency to the Formula 1 standards. Nonetheless, the final cleaned CAD model replicated the overall shape of the surfaces, specifically the floor of the car, to an acceptable accuracy as shown in Figure 4. It was hence expected to see similar flow patterns that illustrate the idea of various flow conditioners and surfaces used by Formula 1 aerodynamicists and how they contribute to the overall performance of the car on the track. Any aerodynamic inefficiency produced by geometrical approximation can also be seen as an opportunity to critique the performance of contributing surfaces.

To transform the published CAD model into a usable CFD model, necessary CAD cleaning was done which included removing all the internal components and creating a closed airtight body. To achieve this, some assumptions had to be made along with some enhancements to the surfaces. These enhancements were sometimes necessary due to faulty readings of some small surfaces during file format conversion, other times were done to correct the shape of some surfaces at critical locations and to ensure the airtightness of the final model sent to the CFD solver. Final CAD model measurements of interest, which were used as a base for the CFD cases are listed below.

- The total length of the car from the foremost point in the front wing to the rearmost point is 5 *m*, 95 *mm*
- The wheelbase was measured to be ≈ 3314 *mm*.
- The maximum width is ≈ 2142 *mm*.
- The front and rear tires both have diameters of 660 *mm* with width of 305 *mm* and 405 *mm*, respectively.
- The ride height of the CAD without any tire deformation and measured to the lowest point in the floor (the plank) is ≈ 60 *mm*

These measurements are all within the 2022 International Automobile Federation (FIA) Technical Regulations [10] except for the maximum width, limited to 2000 *mm*.

CFD Model

Commercial CFD Solver CONVERGE (v3.2.4) [12] was used to build and run the CFD model. Meshing in CONVERGE is done automatically by the solver during runtime using a set of parameters specified by the user, where a base grid size (*dx, dy, dz*) is specified according to Equation (4), for all 3 dimensions. Refinement strategies used in this study are Fixed Embedding, Adaptive Mesh Refinement (AMR), and Grid Scaling with the settings specified in the Meshing section.

$$dx_{refined} = \frac{dx_{base}}{2^n} \tag{4}$$

Where $dx_{refined}$ is the refined spatial discretization cell size, dx_{base} is the base grid cell size, and n is the user input embedding scale.

Reynolds-averaged Navier–Stokes (RANS) Turbulence model $k - \omega$ *SST* was used for this analysis with the recommended values supplied in CONVERGE Studio by default. The automatic wall function in CONVERGE was used for the near-wall treatment of velocity along with the O'Rourke and Amsden's wall heat transfer model [12]. To make use of the symmetricity of the CAD model, the domain was split in half around the symmetry plane of the car to save computational runtime.

Meshing

The results presented in this work used the same mesh control parameters. Zone refinement was automated with the CONVERGE AMR algorithm. The Cartesian grid had a base grid size of *dx* = *dy* = *dz* = 0.2*m*. Fixed embedding boxes A and B were set up to embed cells gradually to the volume near the car.

- Box A, the closest to the car, was centered at (*x, y, z*) = (0, 625, −473) *mm* and had half-length (*dx, dy, dz*)/2 = (5000, 625, 1100) *mm*. The Embed Scale (n) was set to 4, leading to a cell size of 12.5 *mm*.
- Box B had the same center as box A but a half-length (*dx, dy, dz*)/2 = (7500, 1200, 2000) *mm*. The Embed Scale (n) was set to 3, leading to a cell size of 25 *mm*.

AMR was based on the sub-grid scale (SGS) of the velocity. The maximum level of embedding (n) was set to 6 with an SGS value of 0.1 *m/s*. Additionally, to ensure the proper resolution of the boundary layer, Boundary Fixed Embedding was set up on the car walls and wheels with 2, and 3 layers, respectively, and an embedding scale (n) of 8 that leads to a cell size of 781.25*μm*. Finally, automatically-timed grid scaling was applied with 3 scales of –2, –1, and 0 which resulted in a coarse mesh (2 levels relative to the base mesh) at the start of the simulation and refining it subsequently as convergence of flow parameters is achieved. The benefit of this approach is to reduce runtime by coarsening during non-critical simulation times.

Boundary Conditions and Initalization

The computational domain in Figure 5 shows 9 boundaries used in the model. The details of each boundary condition can be explained as follows:

1. Velocity Inlet:
   - Velocity: Constant with a given case speed.
   - Pressure: Zero normal gradient
   - Turbulence: Turbulence intensity of 2% and a length scale of 3 *mm*.
2. Top and Side (Slip Wall):
   - Velocity: Slip boundary condition
   - Turbulence: Zero normal gradients.
3. Symmetry Plane
4. Pressure Outlet:
   - Pressure: 1 *atm*
   - Velocity: Zero normal gradient

FIGURE 5 Computational domain with boundary names (in black) and conditions (in blue)

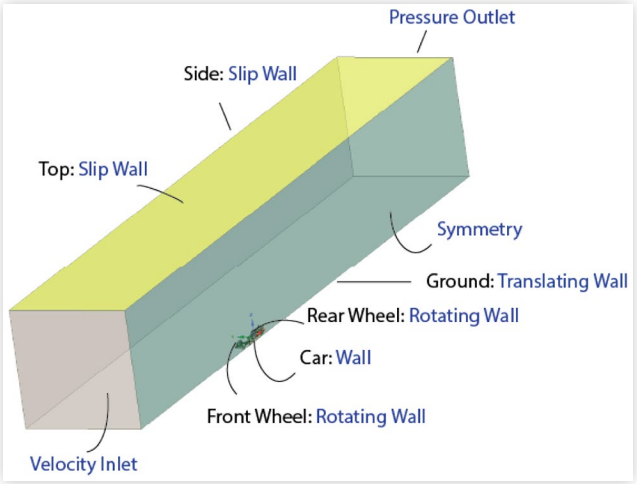

TABLE 2 Boundary Conditions for Cases Included in This Study

Case Number [-]	Inlet Velocity [*m/s*]	Ride Height [*mm*]	Intake/Exhaust Mass Flow Rate [*kg/s*]
1	30	30	0.132
2	30	15	0.132
3	50	30	0.22
4	50	10	0.22
5	90	30	0.4
6	90	5	0.4

   - Turbulence: Turbulence intensity of 2% and a length scale of 3 *mm*.
5. Ground (Translating Wall):
   - Velocity: Translating at given case speed with No-Slip condition.
   - Turbulence: Automatic wall model.
6. Car (Wall):
   - Velocity: Stationary with no-slip condition.
   - Turbulence: Automatic wall model.
7. Front and Rear Wheels (Rotating Walls):
   - Velocity: Rotating Frame of Reference at given case speed about the respective wheel axis.
   - Turbulence: Automatic wall model.

Additionally, two (2) boundaries were defined at the engine intake and the exhaust pipe outlet as mass flow inlet and outlet, respectively. To estimate the mass flow rate and temperatures for these boundaries in each case based on an article published by McLaren Formula 1 team's official website [13] about the engine intake estimate at full speed of 0.4 *kg/s* was used to linearly interpolate an estimate of the mass flow rate through the exhaust and intake. The exhaust temperature was assumed to be constant across all the cases at 1295*K*. The summary of the boundary conditions for all cases is shown in Table 2.

The domain was initialized with the velocity of each case (30, 50, 90) *m/s* in the X-direction). For all cases, The temperature and pressure were set to 300 *K* and 1.01325 *bar*, respectively. Turbulence was initialized in the domain using the Turbulent Kinetic Energy, set at $1 m^2/s^2$, and the Specific Turbulent Dissipation, set at 1000 1/*s*.

Numerical Setup

For all the cases, the Compressible Pseudo-transient steady solver was implemented. The Compressible Pressure-based SIMPLE Navier-Stokes solver scheme was used with 40 maximum number of SIMPLE iterations [12]. Pressure and momentum relaxation factors were set to 0.7 and 0.5, respectively. The energy solver mode was set to solve internal energy. The maximum convection

and mach CFL numbers were set to 10 and 50, respectively, which were generally the limiting factors for the pseudo-timestep. Convergence tolerances for momentum and energy were left as their default values with the pressure convergence tolerance changed to 10^{-8}. All cases were run for a total of 10,000 iterations.

Convergence Criteria

To determine convergence for each case, the mean and standard deviation of the pressure on the car were monitored across the iterations, along with the solver residuals. Convergence was identified when the pressure distribution mean and standard deviation flattened. To do this, a MATLAB code was developed to read the 3D files output by the CONVERGE Solver every 20 iterations, and the pressure calculated on the car surfaces was extracted for each case and plotted. An example of the plot generated for each case is shown in Figure 6.

Grid independence analysis was carried out to ensure the accuracy of the results. This analysis was done on the most critical case of of 90 *m/s* and ride height of 5*mm* by changing the embed level of the AMR and the fixed embedding of Box A and B, whose shapes were explained in the beginning of this section.

Post-processing Approach

Post-processing was mainly done using ParaView v5.11.2. ParaView is an open-source multiple-platform application for interactive and scientific visualization that includes a direct reader of CONVERGE output files [14]. ParaView offers a multitude of 2-D and 3-D visualization tools that facilitated the processing of the simulations carried out in this study. The NVIDIA IndeX for ParaView Plugin [15] was used to process volume data visualization. Additionally, the Line-Integral Convolution (LIC) method, offered through the SurfaceLIC plugin, of the velocity field was used to visualize the vortices circulation regions around the car and underneath the floor.

$$C_P = \frac{\left(P_s - P_{ref}\right)}{\frac{1}{2}\rho_{ref}V_{ref}^2} \tag{5}$$

$$C_{P_T} = \frac{\left(P_t - P_{ref}\right)}{\frac{1}{2}\rho_{ref}V_{ref}^2} \tag{6}$$

Where C_P is the pressure coefficient, P_s is the Static Pressure, P_{ref} is the Reference Pressure, V_{ref} is the Reference Velocity, ρ_{ref} is the Reference Density, C_{P_T} is the Total Pressure Coefficient, and P_t is the Total Pressure

Similar to the static pressure coefficient C_p, defined in Equation 5, the total pressure coefficient C_{P_T} can be defined by substituting the static pressure for the total pressure as shown in Equation 6. If P_{ref} and V_{ref} are chosen to be the free stream pressure P_∞ and velocity V_∞, which is often the case, then in an ideal lossless flow C_{P_T} would be constant at 1 everywhere in the domain. However, since the flow is not ideal, C_{P_T} is very beneficial in identifying lossy areas in the domain for aerodynamic improvements. C_{P_T} can also easily identify vortices cores since the center of the vortex is characterized by a C_{P_T} local minimum.

Due to the nature of the complex flows that arise around a Formula 1 car, it is crucial to use 3-dimensional visualization techniques to be able to trace the effects seen back to their causes. For example, Figure 7 shows streamlines across the longitudinal axis of the car, illustrating the vortices of the rear wing and how their shape is strongly influenced by the flow generated from the front wing and through the side of the car. For that reason, special focus was given to the three-dimensionality of the flow and how various components interact together. This section focuses on the different methods used to achieve that.

FIGURE 6 Example for car surfaces pressure distribution mean μ (solid line) and standard deviation σ (shaded area) against iteration plot

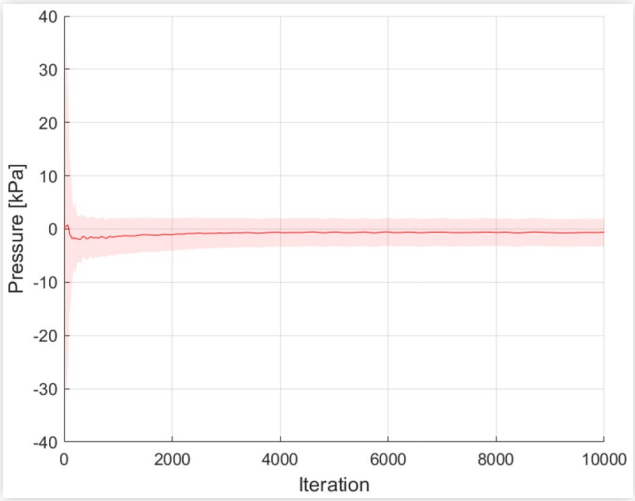

FIGURE 7 Streamlines at 50 *m/s* with 15*mm* ride height showing the rear wing vortices

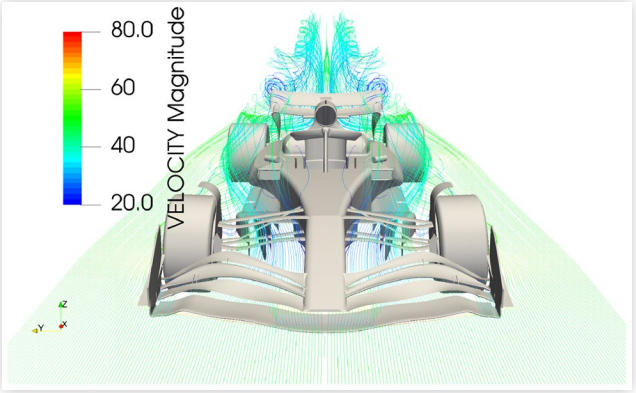

Volume Rendering

Volume visualization involves the process of extracting valuable insights from three-dimensional data through interactive graphics and imaging [16]. This process relies on tracking the path of light rays as they pass through the dataset and is achieved by solving the rendering equation shown in Equation 7 and proposed by Kajiya in 1986 [17]. Hence, to be able to create a volume render, meticulous attention must be given to the color map transfer function and its opacity.

$$I(x,x') = g(x,x')\left[\epsilon(x,x') + \int_S \rho(x,x',x'')I(x'x'')dx''\right] \quad (7)$$

Where $I(x, x')$ is related to the intensity of light passing from point x' to x, $g(x, x')$ is a geometric function, $\epsilon(x,x')$ is related to the intensity of emitted light from x' to x, and $\rho(x, x', x'')$ is related to the intensity of light scattered from x'' to x' by a patch of the surface S at x'.

Volume rendering is a powerful post-processing tool that offers the ability to identify three-dimensional effects in the domain. Nonetheless, limitations to the quality of the output exist. Viewing angle, geometry, cell shape, and the algorithm and method used can create artifacts that are not native to the solution that would appear as a small discolored region or slight discontinuity. This can be more noticeable when the number of cells increases [18]. Fortunately, the method used in this work produced negligible artifacts that did not hinder the overall quality of the results.

Line Integral Convolution (LIC)

This method was proposed by Cabral and Leedom [19] in 1993. The LIC method aimed to visualize vector fields in a way that would be independent of seed points, unlike streamlines and particle tracing which were the basis for methods commonly used at the time [20, 21].

In 1995, the LIC method was further enhanced and named the Fast and Resolution Independent Line Integral Convolution (FastLIC). Unlike traditional LIC, which computes a separate streamline segment and convolution integral for each pixel in the output image, FastLIC introduced significant enhancements to eliminate redundant computations. In the conventional approach, streamlines typically cover multiple image pixels, resulting in frequent recomputation of large sections of streamlines. Additionally, when a constant filter kernel 'k' is applied, similar convolution integrals are computed for pixels along the same streamline, an aspect not fully exploited by traditional LIC.

Convergence Analysis

To ensure solutions are grid independent, the most critical case of 90 *m/s* with low ride height was tested with increasing levels of refinement. The settings for the refinement, compared to the settings previously mentioned in the Meshing section, change the cell embedding scale by (–2, –1, +1) for the Box Fixed Embedding and the AMR, as illustrated and summarized in Table 3, where C_L is the coefficient of lift defined by Equation 8.

$$C_L = \frac{L}{\frac{1}{2}\rho A_{Ref} V_{ref}^2} \quad (8)$$

Where L is the lift force, and A_{Ref} is a reference area taken in this study as $1m^2$ for simplicity. Note that in this case, the terms lift and downforce are used interchangeably.

The error shown in Table 3 shows a small error between the most refined case and the coarsest case. The reason for that is the fact that the variable of interest being monitored is an integral value that could be accurate in a coarser grid. The grid chosen to proceed this study with uses the same parameters as the 8.3 million case parameters.

To analyze the convergence of each steady-state simulation, mentioned earlier in Table 2, the pressure distribution on the car was focused on rather than an integral value like the lift generated. A solution is assumed to have reached a steady state when the mean value and standard deviation of the pressure have converged as shown in Figure 8.

TABLE 3 Grid Independence Analysis

Number of Cells [Million]	C_L [-]	Error [%]	Relative Embed Scale [-]
5.2	5.64	1.24	-2
5.8	5.46	1.84	-1
8.3	5.5	0.684	0
16.1	5.56	-	+1

FIGURE 8 Car surfaces pressure distribution mean μ (solid line) and standard deviation σ (shaded area) against iteration plot for 3 cases: 30 *m/s* at 15*mm* Ride Height, 50 *m/s* at 10*mm* Ride Height, and 90 *m/s* at 5*mm* Ride Height.

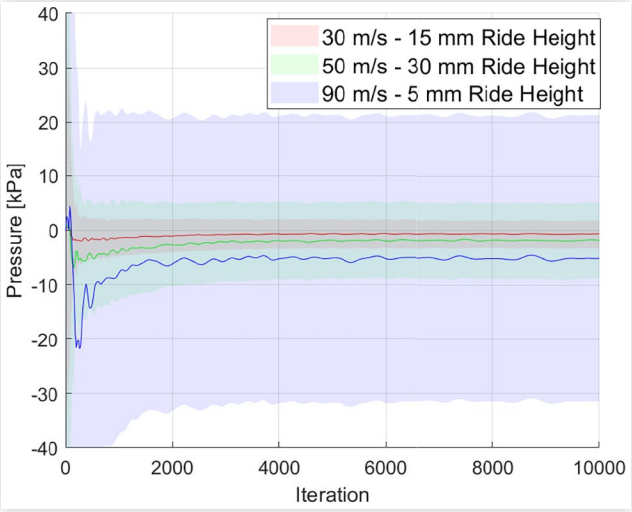

Results

Very complex flow structures arose in the cases investigated. Significant differences were noticed when ride height or speed changes. The diffuser flow structure seemed to be most affected by these changes. Although the flow patterns are highly three-dimensional and the effect of each component is intertwined with the effects of other components, an attempt to break down the results of these complex flows into smaller pieces will greatly help in understanding the contribution of each component individually. Nonetheless, the interaction with other components will be illustrated when necessary.

The next sections will discuss the flow patterns resulting from each source independently. This is achieved by creating three categories: Floor Entrance and Plank Region, Tire Squish Area, and Diffuser Flow. Afterward, an Overall Remarks section is dedicated to compiling the information discussed and their interactions together.

Floor Entrance and Plank Region

The floor entrance region is identified with the bargeboards and the longitudinal strakes. In all the cases studied, the bargeboards appear to have effectively deflected dirty air coming from the inward and outward ends of the tires away from the floor as shown in Figure 9 for all cases. It can also be seen that the bargeboard and the outer strake direct the incoming flow outward, creating a peak suction area in its wake in an attempt to strengthen the vortices produced behind it. This seemed most successful at the inward strake where a strong vorticity region can be seen propagating through the diffuser. Figure 10(e) traces this vortex generated to its origin from the front wing innermost section and shows its expansion in the diffuser.

An interesting behavior in the velocity can be seen at the floor entrance for all low ride height cases shown in Figure 9. A significant drop in the velocity happens that corresponds to an increase in the static pressure shown for the 30 *m/s* 10 *mm* case shown in Figure 11. Additionally, a high vorticity region starts forming near the front portion of the plank at the 50 *m/s* and is seen to increase at the 90 *m/s* with low ride height. This is caused due to the unfavorable flow conditions caused by the positive pressure gradient region that pushes the flow around it and into the floor tunnels. This redirection forms the vorticity region that increases in strength with speed due to the increase in momentum required to be deflected and increases with the decrease in ride height as the restriction on the flow increases. Figure 10(d) shows the

FIGURE 9 Volume render of Normalized Velocity (V/V_∞) and Vorticity Magnitude viewed at floor (Bottom View). The reference line indicates the approximate width of the wake for the 30 *m/s* and 30 *mm* case

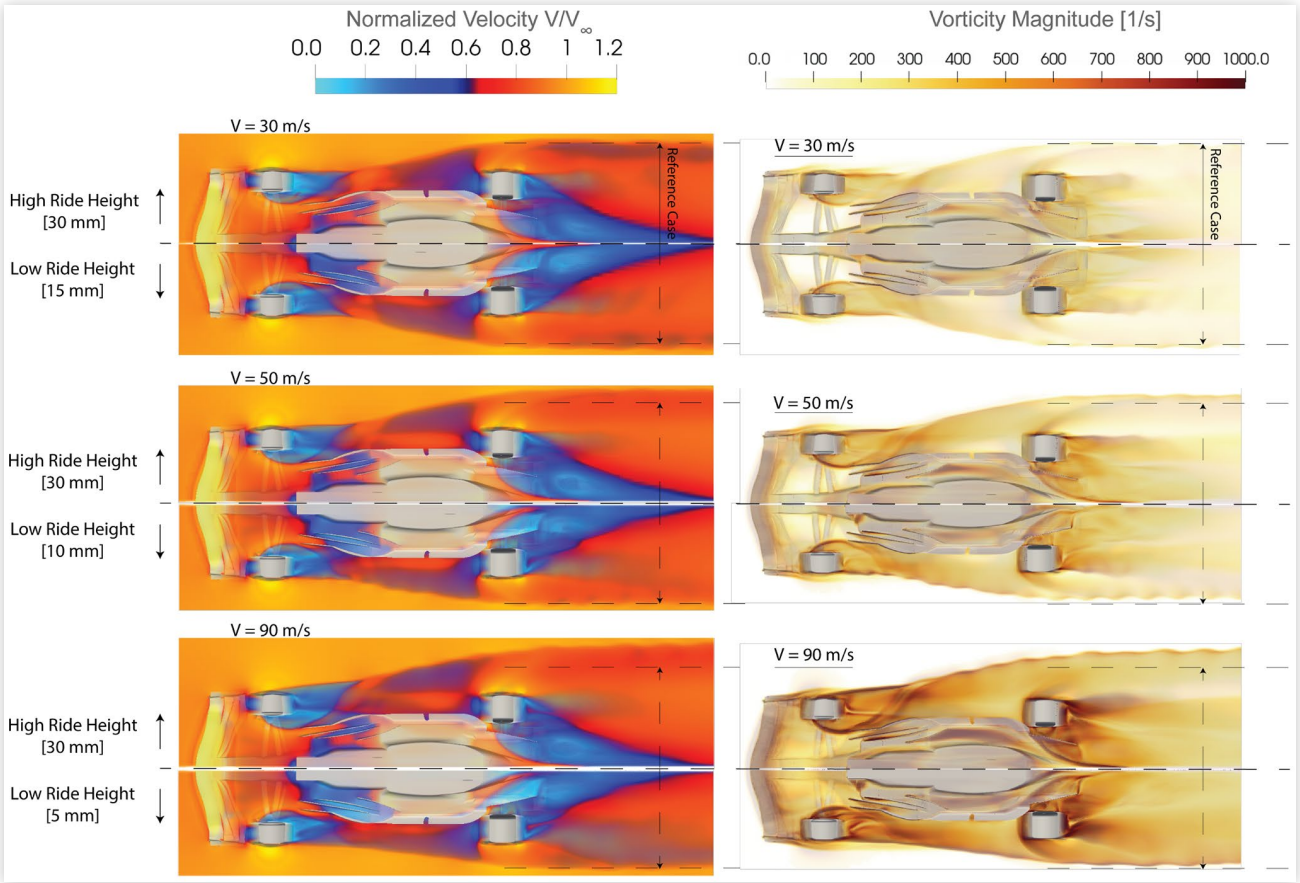

FIGURE 10 Streamlines Representation around the car (a) Compilation of all streamlines from various sources (b) Streamlines of air sucked into the rear end of the diffuser due to separation (c) Streamlines from front and rear tire squirt (d) Streamlines underneath the lowest point in the car (the plank) and the resulting vortex in the diffuser (e) Streamlines of the vortex generated from the strakes at the bargeboard area.

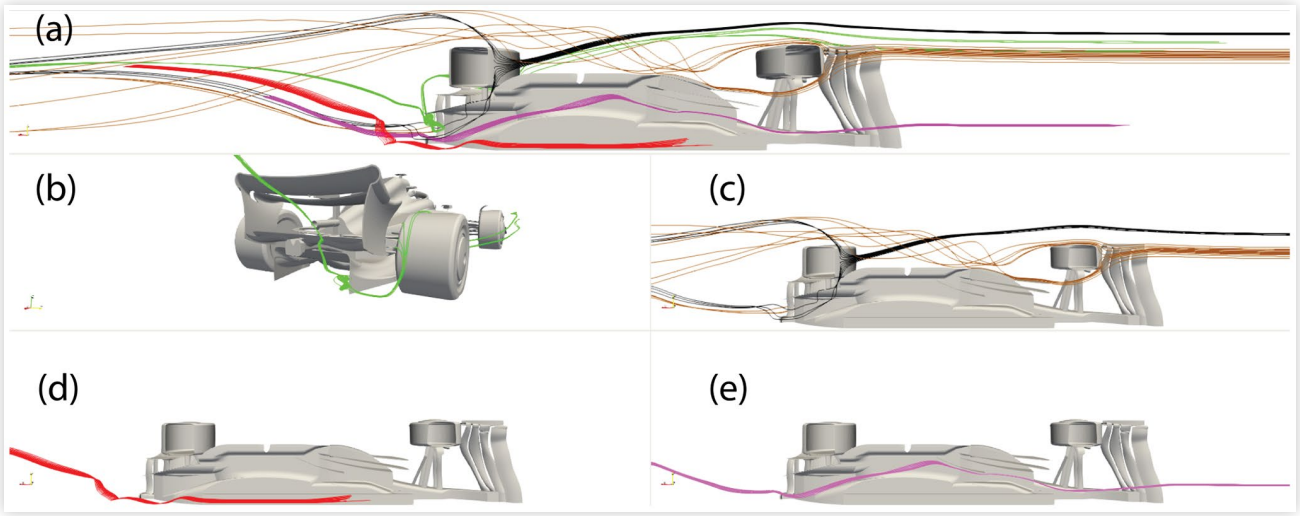

FIGURE 11 Pressure distribution with Velocity LIC lines at 50 *m/s* with 10 *mm* ride height

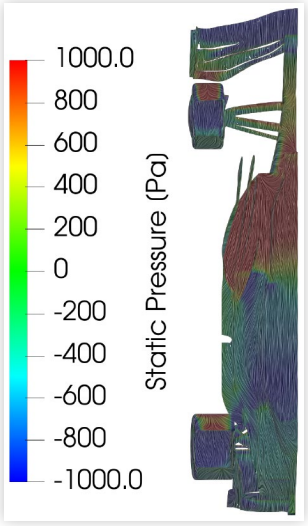

discontinuity in the streamlines that indicates an almost stagnant flow.

Apart from the plank entrance region, the flow seems to continue in a fairly uniform shape, illustrated by the streamlines in Figure 10(d), until it eventually exits through the diffuser where the flow from the plank mixes with the flow from the tunnels creating a rotational area.

Tire Squish Area

Strong vortices are generated at the tire squish area for all cases which can be seen in Figure 9 and Figure 10(c), identified with a high-vorticity-low-velocity region and a significant deflection of the streamlines. The complexity of these vortices structures is directly proportional to the vehicle speed and inversely proportional to ride height. A very noticeable effect is the front tire squish interactions with the bargeboard. The inward vortices are consistently deflected by the bargeboard and are outwashed away from the vehicle. This reflected flow is hit by the vortices from the outer tire squish and the resultant is the outline of the vorticity region observed in Figure 9. This shows the importance of designing the bargeboard in harmony with the wake of the tires. This poses a tradeoff where on one hand keeping dirty air away from the floor is desired while simultaneously trying to minimize the wake width to minimize drag.

At the rear end of the car, the flow produced by the rear tires is left out of the diffuser using the diffuser outer fences, which works similarly to the bargeboard in that regard. However, the rear end of the car has a significantly lower pressure than the front end of the floor, the total pressure itself is expected to decrease as the flow goes further into the region of the car. This can be seen in Figure 14 where the wake of the tire and the inner side of the diffuser have extremely low Total Pressure Coefficient (C_{P_T}) and a significant rotation region illustrated by the LIC lines. These create a strong suction effect that can still draw the air into the diffuser. Additionally, the diffuser exit length is restricted by regulations and does not have the liberty to be extended like the bargeboards. Figure 10(b) illustrates best this effect where an outer streamline that survived the front tire was sucked closer to the car and eventually interacts with the rear tire and gets sucked into the diffuser through its end and recirculates in that region before it is eventually pushed back outside from the rear end of the car.

The open-wheel concept of a Formula 1 car is one of the most difficult challenges and this work shows why. Figure 10(a) shows how all the streamlines that come

FIGURE 12 Plot of C_P, Normalized Velocity (V/V_∞), andWall Shear Stress in the X-Direction (τ_x on the line intersecting the floor of the car and symmetry plane at 50 *m/s* and 10 *mm*)

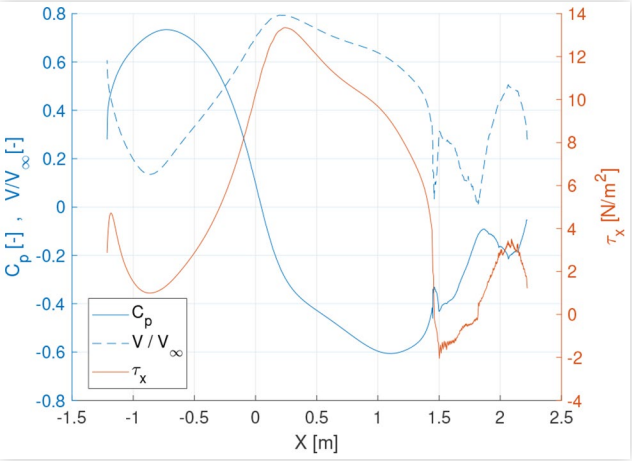

FIGURE 13 Streamlines of flow entering the floor through the side flap for the 50 *m/s* and 15 *mm* case

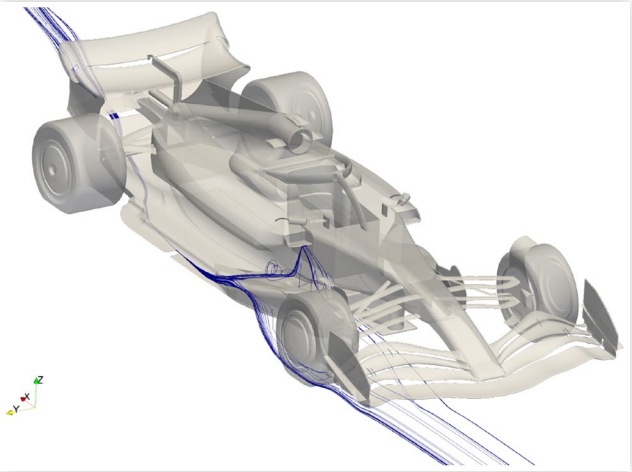

close to the influence region of the tire are being deflected strongly towards the car, thus influencing the performance of many components downstream.

Diffuser Flow

Diffuser performance is pivotal to the overall performance of the floor of the car, and thus, its performance is vital for downforce generation. Separation of the diffuser, for instance, is a common occurrence that can cause a sudden drop in downforce that a driver would feel on the track [22]. Separation of the flow with different degrees can be seen in all cases examined and can be identified by the black recirculation region at the far bottom end of the diffuser in the cases shown in Figure 14. If this same region is examined in the vorticity plots in Figure 9, a strong cross-flow vorticity region can be seen in the low ride height cases that increase in severity as the flow speed increases and the ride height decreases. This can also be illustrated by the streamline shown in Figure 10(b) that got sucked into that region as illustrated above in the Tire Squish Area section. This is generally an unfavorable occurrence that engineers are expected to work hard to avoid.

The plot shown in Figure 12 gives another perspective of the flow at the center of the diffuser. A significant dip in the wall shear stress in the X-direction τ_x occurs at the 1.5 *m* station, which is the area where the flow from the plank area meets the flow from the tunnels and they both enter the diffuser. The sudden change in the geometrical shape of the floor makes this occurrence expected. Nonetheless, the flow reattaches soon after and stays attached until the diffuser exits, albeit decreasing near the end due to the unfavorable pressure gradient that can also be seen in the increase in C_P. This is still deemed a healthy behavior as expanding the flow is the purpose of the diffuser, so long as no separation occurs.

Overall Remarks

Although significant effort has been put into separating the effects of each component individually, it is undeniable that the complex flow structures that arise are all connected and one small change in one component can enhance or deteriorate the performance of another component. Collectively, the goal is to generate downforce with the least possible drag generation. Due to the significant contribution of the floor to achieving this goal, a special focus is understandably put on optimizing it for significant changes with an upgrade. An example of the effect of small geometric features that significantly affect the floor flow is shown in Figure 13 where a small flap strategically positioned on the outer side of the floor allows for flow from multiple regions that experienced chaotic behavior to enter the floor and continue in a structured manner and exit normally through the diffuser.

Conclusions

The geometry and the concepts that a Formula 1 car is built with can result in very complicated flow structures. This work addressed this complexity and illustrated the typical concepts that can be seen in the floor region and how it can be affected by other components like tires, front wing, and side bodywork. To be able to capture the three-dimensional interactions of the car with the flow, techniques like volume rendering, Line Integral Convolution, and streamlines sourced at different locations were utilized to properly assess and understand these interactions. The findings of this work can be summarized as follows:

- The vortices that are shed due to the interaction of air with the tire have a significant effect on the performance of the floor. Undisturbed air passing next to the car can be pulled into the car region because of the front tire wake, which is forced to

FIGURE 14 C_{P_T} and Velocity-based LIC method visualization with high ride height represented on the left-hand side and low ride height represented on the right-hand side (a) 30 *m/s* cases, (b) 50 *m/s* case (c) 90 *m/s* case. (sectional plane location illustrated at the top in black)

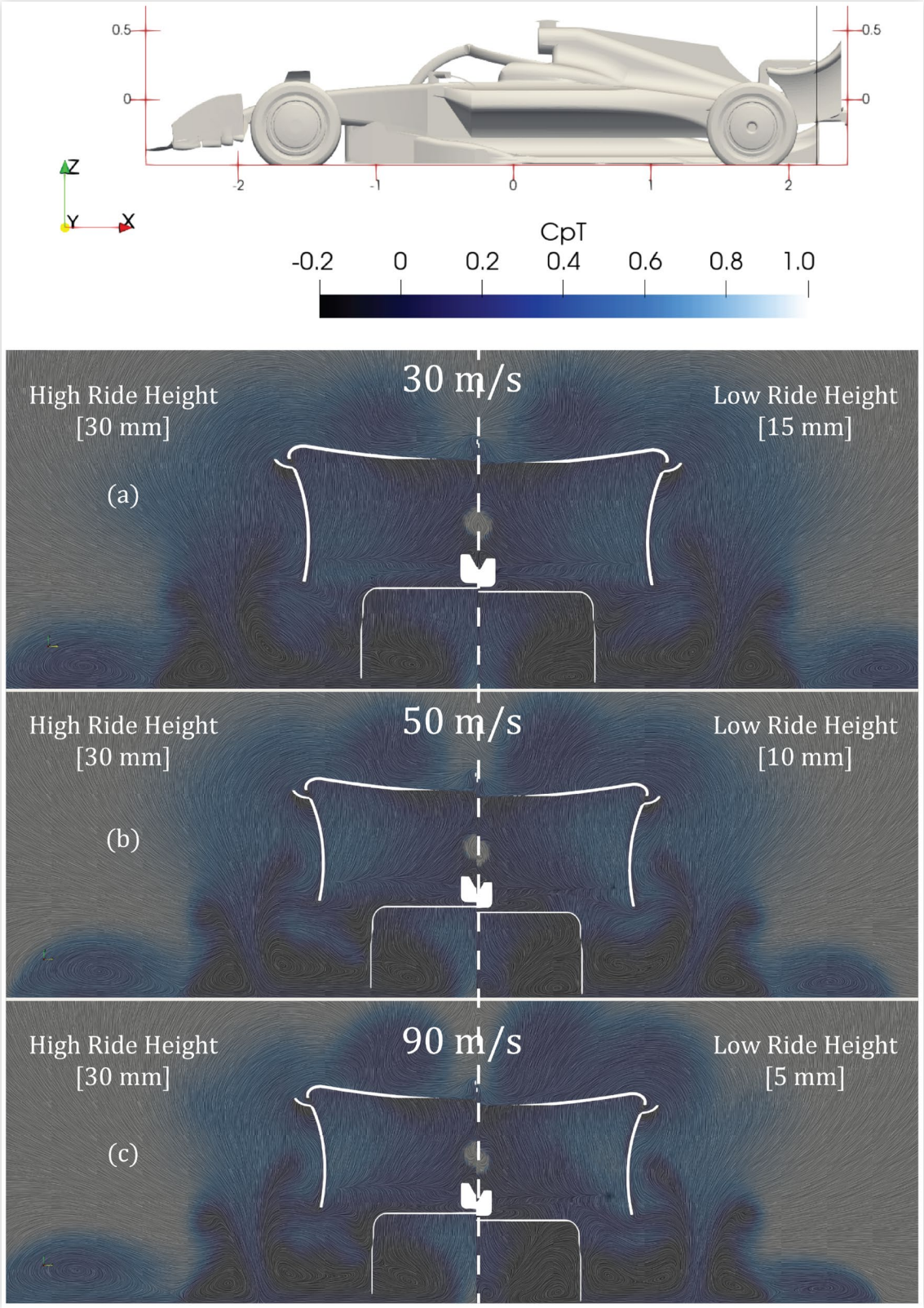

interact with the rear tires and eventually degrade the performance of the diffuser.

- Diffuser separation was seen in this work to be caused by the rear tire wake interaction with the diffuser at low ride heights.
- Ride height significantly affects the pressure distribution at the front of the car, causing a change in the flow path. Generally, the lower the ride height the higher the pressure build-up would occur at the floor entrance. This restriction has a significant effect on the intensity of the vortices shed underneath the car and would therefore need to be accounted for carefully.
- Although the change in airspeed results in a significant change in the pressure and vortices intensity underneath the car, these effects were seen to significantly change when the ride height is also changed. This shows the complexity of the design process and how a lot of effort must be made to calibrate and optimize the car setting for the needs of each track.

References

1. Toet, W., "Aerodynamics and aerodynamic research in formula 1," *The Aeronautical Journal* 117, no. 1187 (2013): 1-26, doi:10.1017/S0001924000007739.
2. Katz, J., "Aerodynamics of race cars," *Annual Review of Fluid Mechanics* 38, no. 1 (2006): 27-63, doi:10.1146/annurev.fluid.38.050304.092016.
3. Katz, J., "Aerodynamics in motorsports," *Proceedings of the Institution of Mechanical Engineers, Part P: Journal of Sports Engineering and Technology* 235, no. 4 (2021): 324-338, doi:10.1177/1754337119893226.
4. Keogh, J., Doig, G., and Diasinos, S., "Flow compressibility effects around an open-wheel racing car," *The Aeronautical Journal* 118, no. 1210 (2014): 1409-1431, doi:10.1017/S0001924000010125.
5. Nitsche, M., "Vortex dynamics," in *Encyclopedia of Mathematical Physics*, Françoise J.-P., Naber G.L., and Tsun T.S., Eds., Oxford: Academic Press, 2006, pp. 390-399, isbn: 978-0-12-512666-3. doi:https://doi.org/10.1016/B0-12-512666-2/00254-6. [Online]. Available: https://www.sciencedirect.com/science/article/pii/B0125126662002546.
6. Ting, D.S.-K., "Chapter 1 - introducing flow turbulence," in *Basics of Engineering Turbulence*, Ting D.S.-K., Ed., Academic Press, 2016, pp. 3-18, isbn: 978-0-12-803970-0. doi:https://doi.org/10.1016/B978-0-12-803970-0.00001-5.
7. Kundu, P.K., Cohen, I.M., and Dowling, D.R., "Chapter 5 - vorticity dynamics," in *Fluid Mechanics (Sixth Edition)*, Kundu P.K., Cohen I.M., and Dowling D.R., Eds., Sixth Edition, Boston: Academic Press, 2016, pp. 195-226, isbn: 978-0-12-405935-1. doi:https://doi.org/10.1016/B978-0-12-405935-1.00005-8.
8. Kallweit, S., Michaux, F., Hojo, T., and Nakagawa, M., "Typical velocity fields and vortical structures around a formula one car, based on experimental investigations using particle image velocimetry," *SAE International Journal of Passenger Cars – Mechanical Systems*, vol. 9, no. 2, pp. 754-771, Apr. 2016, issn: 1946-3995. doi:https://doi.org/10.4271/2016-01-1611.
9. Loots, S., *Formula 1 car 2022 version 1.1*, Jul. 2022. [Online]. Available: https://grabcad.com/library/formula-1-car-2022-version-1-1-1.
10. (FIA), I. A. F., "2022 formula 1 technical regulations," 2021.
11. Valantine, H., *Sergio perez addresses rumours of intentional crash at monaco gp*, Nov. 2022. [Online]. Available: https://www.planetf1.com/news/sergio-perez-intentional-monaco-crash.
12. Richards, K., Senecal, P., and Pomraning, E., *Converge* (2023).
13. Oct. 2013. [Online]. Available: https://www.mclaren.com/racing/latest-news/mclarenracing/article/f1s-fantastical-facts/.
14. *Paraview guide, a parallel visualization application. kitware inc., 2007*, Accessed: 2023-10-30. [Online]. Available: http://www.kitware.com/products/paraview.html.
15. *Nvidia index for paraview plug-in*, Accessed: 2023-10-30. [Online]. Available: https://www.nvidia.com/en-us/data-center/index-paraview-plugin/.
16. Kajiya, J.T., "The rendering equation," *SIGGRAPH Comput. Graph.*, vol. 20, no. 4, pp. 143-150, Aug. 1986, issn: 0097-8930. doi:10.1145/15886.15902. [Online]. Available: https://doi.org/10.1145/15886.15902.
17. Kajiya, J.T., "The rendering equation," in *Proceedings of the 13th Annual Conference on Computer Graphics and Interactive Techniques*, ser. SIGGRAPH '86, New York, NY, USA: Association for Computing Machinery, 1986, pp. 143-150, isbn: 0897911962. doi:10.1145/15922.15902.
18. Kaufman, A.E. and Mueller, K., "Overview of volume rendering," *The visualization handbook* 7 (2005): 127-174.
19. Cabral, B. and Leedom, L., "Imaging vector fields using line integral convolution," in *Seminal Graphics Papers: Pushing the Boundaries, Volume* 2, 1st ed. New York, NY, USA: Association for Computing Machinery, 2023, isbn: 9798400708978. doi:10.1145/3596711.3596752.
20. Kenwright, D.N. and Mallinson, G.D., "A 3-d streamline tracking algorithm using dual stream functions," in *Proceedings of the 3rd Conference on Visualization '92*, ser. VIS '92, Boston, Massachusetts: IEEE Computer Society Press, 1992, pp. 62-68, isbn: 0818628960.
21. Tufte, E.R., *The visual display of quantitative information* (Graphics Press, 2018)
22. Milliken, W.F. and Milliken, D.L., *Race Car Vehicle Dynamics* (SAE International, 1995)

Contact Information

Amr Shaalan
(amr.shaalan@stonybrook.edu)
Graduate Student Research Assistant
Dept. of Mechanical Engineering
Stony Brook University
131 Light Engineering
100 Nicolls Rd
Stony Brook, NY 11794
USA

Prof. Dimitris Assanis
(dimitris.assanis@stonybrook.edu)
Assistant Professor
Dept. of Mechanical Engineering
Stony Brook University
131 Light Engineering
100 Nicolls Rd
Stony Brook, NY 11794
USA

Acknowledgments

The computational studies and analysis were performed at the Advanced Combustion & Energy Systems Laboratory located in the Advanced Energy Research and Technology Center at Stony Brook University in Stony Brook, NY. The authors would like to also thank Stony Brook Research Computing and Cyberinfrastructure and the Institute for Advanced Computational Science at Stony Brook University for access to the SeaWulf computing system, which was made possible by a $1.4M National Science Foundation grant (#1531492). The authors additionally thank Convergent Science for providing CONVERGE licenses and technical support for this work.

Definitions, Acronyms, Abbreviations

CFD - Computational Fluid Dynamics

CAD - Computer-Aided Design

LIC - Line Integral Convolution

AMR - Adaptive Mesh Refinement

ISSN 0148-7191